

Investigation of Photocurrent Losses in Pyrite (FeS₂) Film Consisting Single Crystal Nanocubes

Sudhanshu Shukla¹, Thirumany Sritharan², Xiong Qihua³, Tze Chien Sum³, Guichuan Xing³, Nripan Mathews^{1,2}, Hu Ge², Thirumalai Venkatesan^{4,5}, Sinu Mathew^{4,5}, Su Zhenghua¹, Venkatram Nalla⁶

¹Energy Research Institute, Nanyang Technological University
Nanyang Avenue, Singapore

²School of Materials Science and Engineering, Nanyang Technological University
Nanyang Avenue, Singapore

³Division of Physics and Applied Physics, School of Physical and Mathematical Sciences,
Nanyang Technological University
Singapore

⁴Department of Electrical and Computer Engineering, National University of Singapore
Singapore

⁵NUSNNI-Nanocore, National University of Singapore
Singapore

⁶Centre for Disruptive Photonics Technologies, National University of Singapore
Singapore

assritharan@ntu.edu.sg

Abstract – Successful extraction of photo excited carriers from a photo active material is key towards a successful PV device. The high losses exhibited by a device with pyrite as the active layer has been noted previously but never investigated systematically to understand the photo physics and the carrier loss mechanisms to improve its performance. Here we report a detailed characterization of a film made using {100} terminated, pure pyrite single crystal nano cubes. Using ultrafast transient absorption spectroscopy we found fast carrier localization of photo excited carriers to indirect band edge and shallow trap states with characteristic decay time of 1.8 picoseconds, followed by relaxation to deep states and recombination of trapped carriers with long characteristic decay times of 50-990 nanoseconds. Its optical absorption characteristics correlate to a disordered semiconductor. Temperature dependent electrical resistivity exhibits a Mott - variable range hopping (VRH) type conduction mechanism consistent with the presence of high density of defect states. An electron band model with midgap defect states is formulated that could explain all the observed phenomena.

Keywords: nanocubes, optical transient absorption spectroscopy, variable range hopping, magnetization, carrier dynamics

1. Introduction

The major impediment to widespread solar energy conversion is the high cost of the modules as well as the requirement for large areas of land. Consequently, the motivating factor for photovoltaic (PV) research has been to achieve high efficiency at low cost with environmentally benign materials [1,2]. Earth abundant semiconducting materials such as CZTS, CuO, Cu₂O, Cu₂S, CoO₃, Zn₃P₂ and FeS₂ offer great potential in this respect [3]. Of these, FeS₂ (pyrite) has received interest due to its abundance and attractive optical properties. It has a remarkably high optical absorption coefficient ($\alpha > 10^5$ cm⁻¹ for $h\nu > 1.3$ eV), a good energy band gap E_g of ~ 0.95 eV and sufficiently long minority carrier diffusion length (100 nm – 1000 nm). Besides, a high carrier mobility of $\mu \sim 360$ cm² V⁻¹ s⁻¹ has been reported for n-type bulk single crystals [4]. Nonetheless, the efficiency for a pyrite single crystal photoelectrochemical cell could not exceed 2.8 % with an extraordinarily high short circuit current ($J_{sc} = 42$ mA/cm²) and fill factor of 50 %. This low efficiency is attributed to its low open circuit voltage of $V_{oc} \sim 187$ mV which has still not been surpassed, even after nearly 30 years of the first report by Tributsch and co-workers [4]. All previous researchers attributed the problem of low photo voltage to defect states within the forbidden energy gap caused by of phase impurities and stoichiometric deviations in the pyrite.

Recently, independent studies from Jin et al [5,6] and Law et al [7,8] propose the existence of a surface charge inversion layer and conclude that the surface states and ionization of high density deep donor defect states are responsible for low voltages. Interestingly, recent reports of synthesis of pure pyrite nanostructures by solution processing [8-11] provides the means to avoid impurities and surface inversion problems in pyrite. They offer a unique platform to study fundamentals as well as device physics due to their better control of quality, composition, size and shape, and the relative ease of making films by simple dip or spin coating. However, post treatment is generally required to remove any residual organics, before device applications to get appreciable currents in films through enhanced electronic inter-particle coupling [12]. Nanostructured iron pyrite has been tested in many optoelectronic devices [13-19] but did not prove their effectiveness in solar cell configurations which is a setback. Despite this, we believe that the high responsivity to optical excitation, coupled with good crystallinity and stability, would be still advantageous for use as the absorber layer in solar cells if adequate photo voltage could be derived. To achieve this, the physics of photo excitation and charge carrier dynamics in pyrite must be well understood.

In this work, we investigated the charge carrier generation and relaxation dynamics in as-prepared and sulfur treated {100} faceted iron pyrite nano cubes by ultrafast transient absorption (TA) measurements. Since {100} surface inhibits surface reconstruction, contrary to {111} or {210} face, {100} faceted nano cubes are chosen for the present study [20-22]. From a variety of investigations to monitor and characterize the effects of crystal defects, a carrier relaxation model is proposed where the relaxation pathway is through multiple electronic transitions within the band gap. Passivation of these mid gap states might enable adequate increase in the photo voltage of pyrite nano-crystalline solar cells to make them commercially competitive.

2. Methods

Pyrite nano cubes were synthesized by a hot injection method starting from FeCl_2 and elemental sulphur powder. The details are described in our previous publications [11,23]. 50 μL suspension of pyrite in ethanol, at a concentration of 0.1M, was used to spin-coat on glass substrate. The coating was done sequentially to get adequate film thickness of about 300 nm. This is termed the as-prepared film. Some of the as-prepared samples were sulphurized in a two-zone furnace with sulphur powder at the colder zone of 200° C while the film was kept at 500° C in an argon atmosphere for 30 mins. This was done to remove remnant organic ligands on the cubes from the synthesis process and to improve inter-particles electrical contact. The furnace tube was evacuated and purged with argon three times before this sulfurization process to ensure a clean argon atmosphere and to avoid any oxidation of pyrite.

The films were characterized by X-ray diffraction (XRD) and high resolution transmission electron microscopy (HRTEM) for crystallinity and phase purity. Since the sensitivity of the XRD in detecting small fractions of impurity phases is limited, confocal micro-Raman with laser excitation at 532 nm with 0.14 mW power was resorted to, to confirm the crystal purity. Subsequently, optical absorption (UV-Vis absorption spectrophotometer), electrical and magnetic properties were evaluated. To elucidate the effects of defects on charge carrier dynamics, ultrafast laser pump-probe, transient absorption (TA) spectroscopy was done on both as-synthesized and sulfurized samples. The broad band dynamical TA spectra were collected in nanosecond and microsecond probe time delay range with Ultrafast System HELIOSTM and EOSTM, respectively.

3. Results and Discussion

Figures 1(a) and 1(b) show the XRD data and Raman spectra of as-prepared and sulfurized films, respectively. All XRD peaks could be indexed to the cubic pyrite phase (JCPDS 42-1340). No peaks from potential impurity phases such as pyrrhotite (Fe_{1-x}S), iron monosulfide (FeS), marcasite (orthorhombic polymorph of FeS_2) or iron oxide were detected. It is evident from these figures that sulfurization process retains the shape and phase purity of the as-synthesized sample. Lattice constants computed for the as-coated and sulfurized films from the XRD spectra are 5.392 Å and 5.412 Å respectively. This is very close to the value of 5.418 Å reported for a high quality, pyrite sample [24].

Three characteristic phonon modes were observed in the micro-Raman spectra at wavenumber 341 cm^{-1} (A_g), 377 cm^{-1} (E_g) and 425 cm^{-1} ($T_g(3)$) respectively. The A_g and E_g modes are from sulfur-sulfur bond vibrations and $T_g(3)$ is vibrational mode [25,26]. Out of five Raman active modes, the $T_g(1)$ and $T_g(2)$ phonon modes are generally not observed due to significant light extinction caused by other modes and inefficient light scattering at room temperature [27]. Both as-prepared and sulfurized films showed only pyrite peaks confirming the high phase purity of the films.

Nanocube morphology of as-prepared and sulfurized films is evident from SEM micrographs of Figures 1(c) and 1(d) with clear facets. The single crystalline quality and phase purity were confirmed by HRTEM as shown in Figure 2. Every nano cube is a single crystal. Lattice resolved high resolution image of Figure 2(b) yields a lattice constant of 5.48 Å, in congruence with the (100) plane lattice spacing. Selected area diffraction (SAED) pattern of Figure 2(c) shows two pairs of planes which could be indexed to (200) & (-200) and (020) & (0-20). The zone axis of the cube is [001] direction. This proves that the nano cubes are terminated with {100} facets. Planar defects such as stacking faults could be discerned in the lattice as marked with yellow lines and arrows in Figure 2(b). Although, such defects have been previously reported in nanoparticles, their presence in this study is significant as they may have a critical role in governing the electronic properties of pyrite nanoparticles [10,28,29].

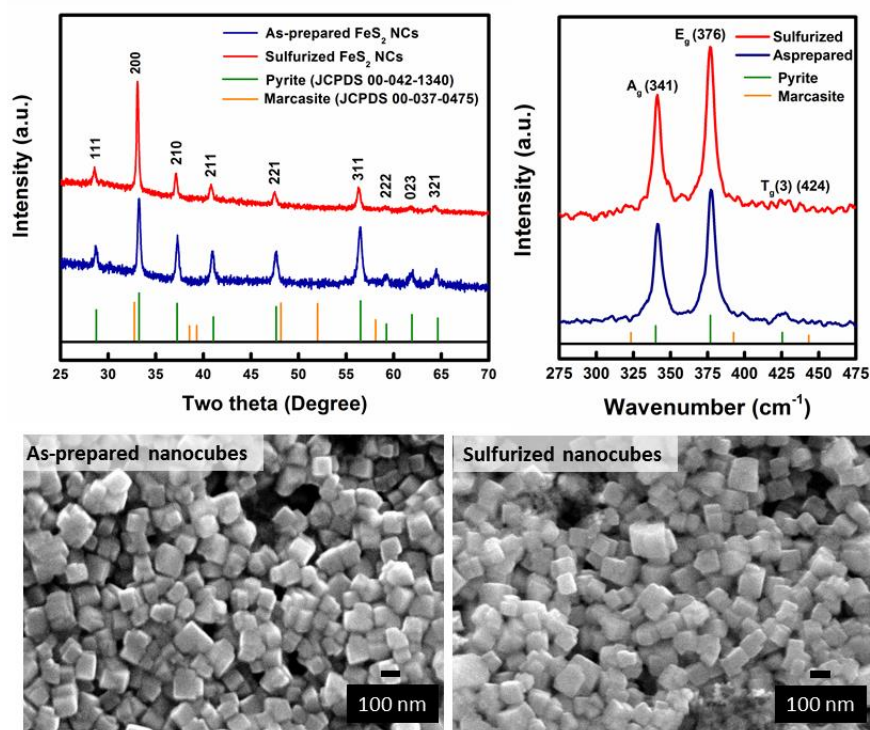


Fig. 1: Structural characterization. (a) XRD pattern, (b) Confocal micro-Raman spectra, and SEM micrographs of (c) as-prepared and (d) sulfurized pyrite nanocube films.

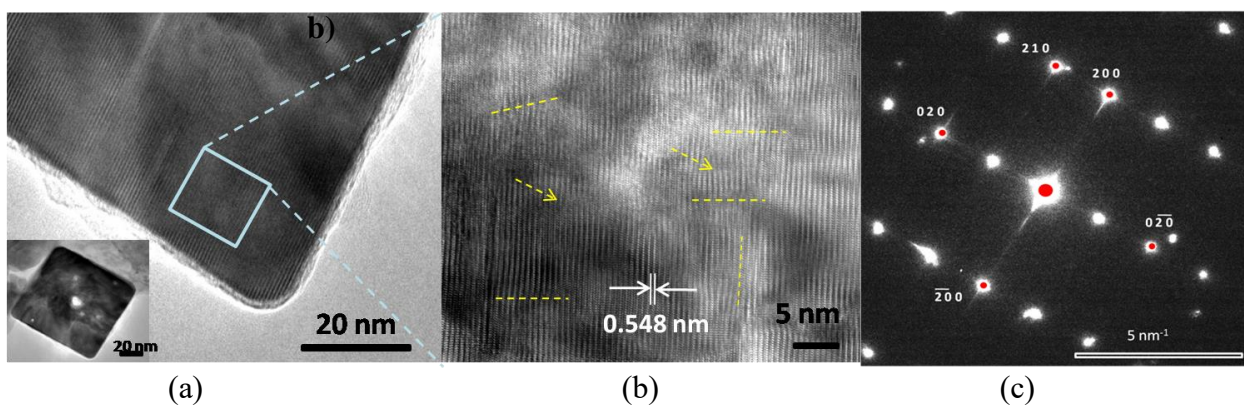


Fig. 2: HRTEM image of iron pyrite nanocube. (a) Edge of the nanocube, inset shows full nanocube image, (b) lattice fringes and stacking faults marked with yellow dashed lines and arrows and (c) selected area diffraction (SAED) pattern indicating the points corresponds to marked planes (red spots).

Optical absorption spectra of the films is shown in Figure 3(a) and 3(b). An optical absorption coefficient $\alpha > 1 \times 10^5 \text{ cm}^{-1}$ for $h\nu > 1.3 \text{ eV}$ was obtained. Such a high optical absorption is a trait of iron pyrite. Optical band gap of the material was analyzed by a Tauc plot in Figure 3(c). Regions of different slopes could be identified in this plot, which could correspond to optical excitations from band edges and defect states/bands. Intercepts of the linear extrapolations of the different slopes in the plot on the energy axis could be interpreted as optical transitions corresponding to those specific energy levels. Electronic behavior of pyrite is governed by these energy level transitions. Three such distinct energy transitions could be identified at 1.1 eV, 1.5 eV and 1.9 eV in Figure 3(c) although all the tangents are not drawn. The estimated band gap is 1.1 eV which is well within the range (0.80 eV to 1.10 eV) commonly reported for pyrite [4,22,30]. However, this band gap value appears to be direct as it fits linearly with $n = 2$ value in the parameter $(\alpha h\nu)^n$ in the Tauc equation. Such indirect to direct transition is not unusual in semiconductors with high density of defect states and disorder, and has been reported even for pyrite single crystals [5]. A possible optical transition at 1.5 eV corresponds to the fundamental direct band to band excitation, consistent with previously reported values [31,32]. The third probable transition could be obtained at 1.9 eV agrees well with values approximated by theoretical study and experimentation and could be attributed to the interband excitonic transition [22,33,34]. Notably, the discrepancies in commonly reported optical band gap of pyrite could be an indication of the presence of fuzzy band edges in pyrite, a common feature in disordered semiconductors. Potential fluctuations arising from defects perturb the electronic band edges and could result in broadening of electronic states leading to band tails extending below the band edges, which could manifest as sub-band gap optical absorption [35,36]. The absorption spectra in Figure 3(a) could be divided in four regions. The region I could be attributed to optical transition from extended states to mid-gap localized states; region II to exponential tail due to transitions from one of the extended states to the another band tail localized states at absorption edge; region III could be due to power law dependence of absorption coefficient on photon energy; region IV could be the fundamental optical absorption. For pyrite, the defects may be intrinsic, such as sulfur and iron vacancies that have been predicted by first principle studies [37,38].

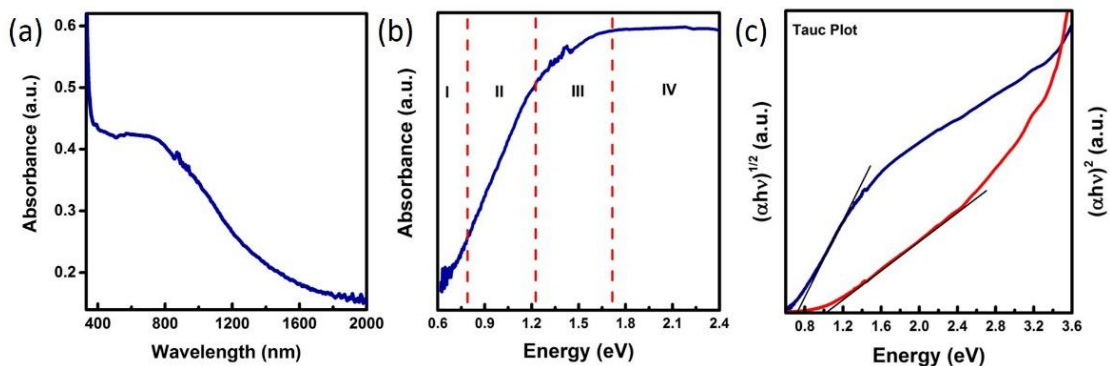


Fig. 3: (a,b) UV-Vis absorption spectra and (c) Tauc plot analysis of; as-prepared and sulfurized iron pyrite nanocubes.

Ultra-fast pump-probe TA spectroscopy allows us to monitor the charge relaxation process in the samples. Following photoexcitation with 900 nm and 1600 nm pump pulses, the hot charge carriers rapidly relax to the band edge and trap states. Figures 4(a) and 4(c) show the pseudo color plots of the change in absorption, ΔA (represented by the color scale) in plots of wavelength (nm) against probe time delay for the sulfurized sample. The data for as-prepared sample was similar and hence is not given here. Similarity of the spectra for the as-prepared and sulfurized samples proves that the intrinsic electronic property of pyrite was not changed by sulfurization. Figure 4(a) shows a prominent negative ΔA band or photobleaching (PB) signature near the bandgap at around 950 nm. This PB shows a fast decay with probe delay time as in Figure 4(b). Fitting a single exponential decay curve to the data gives a characteristic time constant of 1.8 ps. This lifetime closely matches with the building up time of a broad positive ΔA band or photo-induced absorption (PIA) signature at wavelengths $>1000 \text{ nm}$. Hence, this band edge PB signal should originate from stimulated emission of the photo-generated carriers near the bandgap and filling of the band edge states. The broad PIA band below band gap should originate from the localized charge carrier absorption. Therefore, the band edge PB fast decay represents photo-generated charge carrier localization from the direct gap edge to indirect band edge and middle gap trap states. Considering the p-type nature of the

sample, this fast charge carrier localization possibly originates from the photo-generated electron localization and trapping. The recombination time of the trapped electrons with holes is in few hundreds of ns as evident in Figure 4(d). Based on our reasoning for the fast and slow carrier decay times, we have formulated representative photo physical processes schematically in Figure 5. These processes clearly indicate the high carrier losses in iron pyrite due to fast localization and recombination assisted by intermediate gap states.

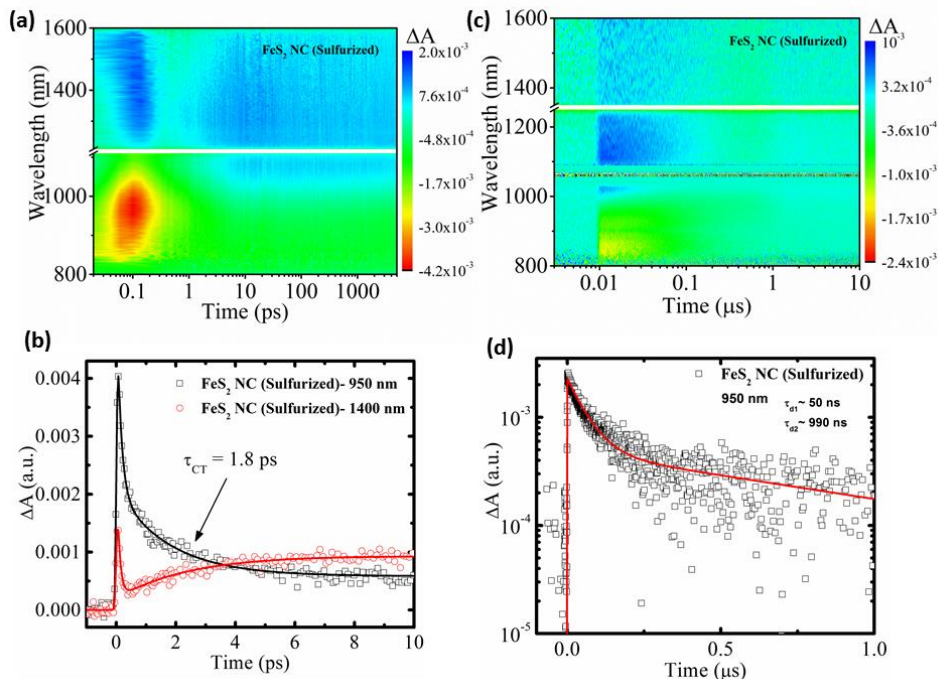


Fig. 4: Differential absorption spectra after photoexcitation as a function of time delay in (a) femto-pico second range, (c) nano-micro second range. Carrier decay dynamics probed at 950 nm (photobleaching) and 1400 nm (photoinduced absorption) by fitting the transients in (b) picosecond range, fitted with single exponential decay function (solid black line) with decay time constant (charge transfer time, τ_{CT}) 1.8 ps and (d) microsecond range, fitted with biexponential decay function with time constants 50 ns (τ_{d1}) and 990 ns (τ_{d2}) associated with long live trap states and recombination process.

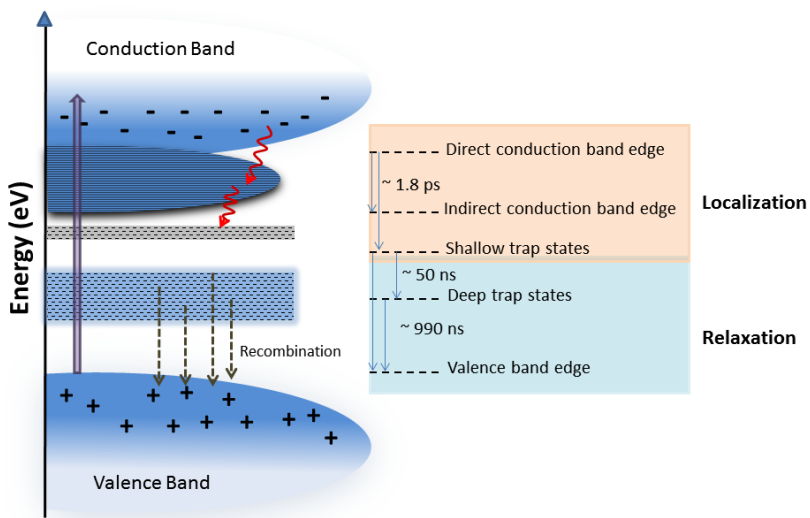


Fig. 5: Representative schematic of the photophysical processes involved in iron pyrite. The energy axis is arbitrary and the mechanism shown is based on the results obtained from optical pump probe spectroscopy.

Next, we examine the impact of such high defect states on charge carrier transport in pyrite which is necessary to understand the performance of pyrite based solar cells. To study the physics of carrier transport and intrinsic defects, we conducted temperature dependent electrical transport and magnetic measurements. Figure 6(a) shows the dependence of resistivity ($\text{Ln } \rho$) on $1/T$ (inset shows the resistance *versus* temperature raw data) which resembles a typical semiconducting behavior. When the results are plotted against $T^{-1/4}$ a straight line could be fitted from room temperature (300 K) to about 50 K as shown in Figure 6(b). This indicates a good agreement with Mott variable range hopping (VRH) mechanism for charge transport given by the equation $\rho = \rho_0 \exp(T_0/T)^{1/d+1}$. d in the exponent is the dimensionality of the system, T_0 is the characteristic temperature and ρ_0 is a weak temperature dependent pre-exponential factor (value of ρ at $T \rightarrow \infty$) which depends on the electron-phonon interactions [39]. A high characteristic temperature of $T_0 = 4.5 \times 10^6$ K obtained by linear fitting of $\text{Ln } (\rho)$ vs. $T^{-1/4}$. Such type of conducting behavior is marked by charge transport through the localized states *via* phonons (phonon assisted transport). At finite temperature, VRH conduction is caused by the localized states that depend on dimensionality (d) of the system [40]. Since the charge transport in our films is through nano cubes, the value of $d = 3$ could be assumed due to 3- dimensional isotropy of nano cubes. This argument agrees well with the experimental data fitted with 3- dimensional VRH equation.

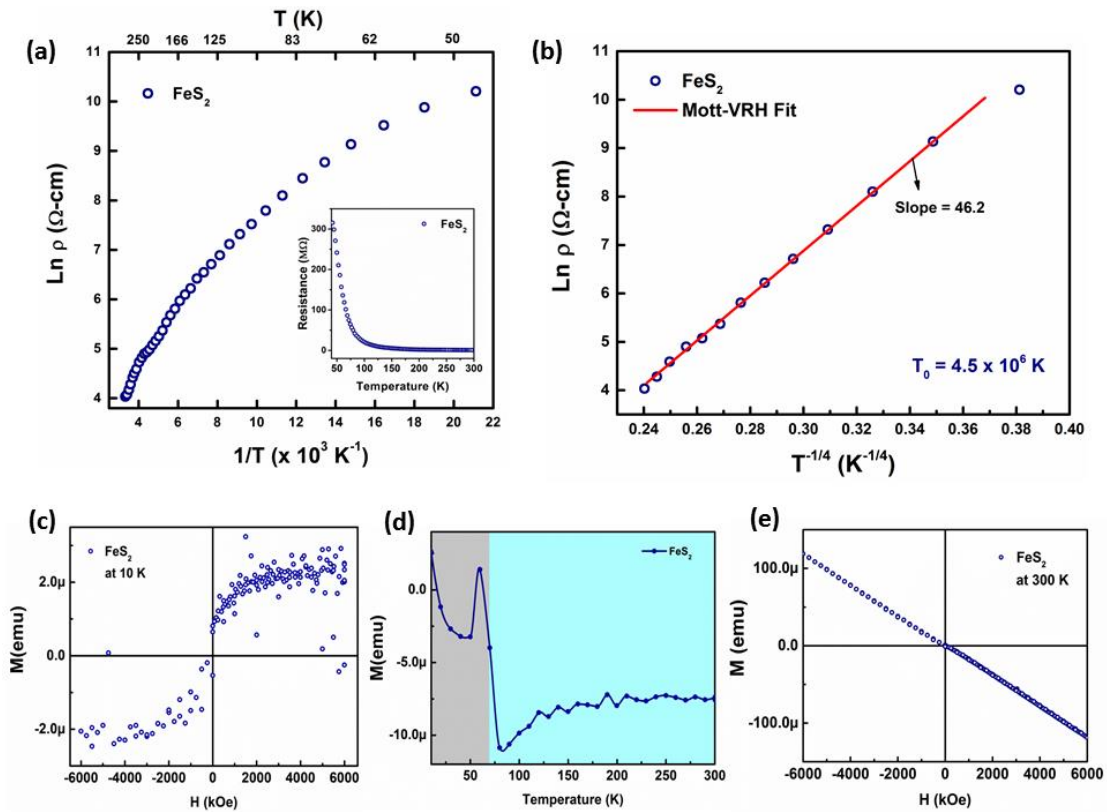


Fig. 6: Electrical transport of iron pyrite, (a) Logarithm of resistivity vs $1/T$ plot. Inset shows resistance vs temperature plot, (b) $\text{Ln } \rho$ vs $T^{-1/4}$ plot fitted linearly with Mott-VRH type transport. Magnetic measurements on iron pyrite, (c) M - H curve at 10 K showing superparamagnetic response with finite saturation magnetization, (d) Magnetization vs temperature plot from 300 K – 10 K and (e) M - H curve at 300 K showing diamagnetic response.

Previous transport studies on iron pyrite single crystals and nanostructures also showed Mott-VRH type conduction phenomena [5,41]. The fact that Mott-VRH type conduction behavior is often observed in different pyrite nanostructures, regardless of synthesis procedure, reinforces the existence of smaller localization lengths and intrinsic defect mechanisms in all pyrite samples. The presence of high density of defect states reflected by our optical pump probe studies is in agreement with the charge transport behavior observed in the temperature dependence of resistance in the iron pyrite films. It is thus clear that the disorder and intrinsic defects in the pyrite crystals create the defect states that trap the charge

carriers and consequently assist in recombination. Intrinsic defects are arguably the most plausible explanation for the universal conduction behavior of pyrite and its sluggish photo response.

We conducted temperature dependent magnetic measurements also on our iron pyrite film samples. As shown in Figure 6(c) the film shows a weak magnetic ordering at 10 K with a clear saturation magnetization. Temperature dependent magnetization data is shown in Figure 6(d) which indicates enhanced magnetization at temperatures below 50 K. On the other hand, at room temperature, pyrite is non-magnetic (diamagnetic) as evident from the magnetization curve of Figure 6(e) as reported by others because it has electrons filled in t_{2g} state in low spin configuration [42,43]. Many other Fe and other Fe-S phases exhibit magnetic order. However, our phase identification investigation showed the absence of any impurity phases. This raises the possibility of unexpected phases such as $Fe_{\delta}S_{1-\delta}$ ($0 \leq \delta \leq 1$) being formed at localized regions at low temperatures due to condensation of sulfur vacancies within the bulk and the surface. This could happen when the point defects order to low energy configurations at low temperatures, which could create nano-scale regions of non-stoichiometry, and consequently magnetic ordering at such localities. At higher temperatures, such defects are randomly distributed and hence do not influence the bulk magnetic behavior. Since point defects are a source of localized gap states, the magnetic information also strengthens photo physical processes formulated in Figure 5.

4. Conclusions

We have studied high purity, as-prepared and sulfurized iron pyrite films consisting of nano cube shaped single crystals, prepared by hot-injection method. Its optical absorption corresponds to that of a disordered semiconductor. Optical pump-probe transient absorption spectroscopy showed both photo carrier generation and relaxation processes. Strong photo carrier generation occurs at direct band edge (~ 950 nm). Relaxation of the photo excited carriers consisted of a fast and a slow components. The fast component could be assigned to rapid carrier localization of the excited carriers to indirect band edge and shallow defect states with a characteristic decay time of 1.8 ps. The slow component could be attributed to carrier relaxation through deep, mid gap states, and recombination via direct hole capture process. Temperature dependent transport measurements showed VRH type conduction from 50 K - 300 K. Temperature dependent magnetic measurements showed magnetic ordering appearing at temperatures < 50 K in contrast to diamagnetic behavior at room temperature. All these findings are consistent with the presence of a high density of defect states.

We believe good photo voltages can still be obtained from the pyrite films made here if we could achieve two improvements: (i) Enhancement of inter-particle electrical coupling or realizing a single domain film, free of boundaries; (ii) Mitigating the defect states present within the band gap by using crystal growth strategies and post treatments to limit the bulk defects, as bulk defects would be a major impediment for the enhancement of photo voltage. We believe our findings will help to understand the rarely explored photo physics of iron pyrite and provide deep insight to the inter-relationship between crystal defects, gap states and photo carrier losses.

Acknowledgements

Authors would like to thank funding by the National Research Foundation, Singapore under their CREATE program Singapore-Berkeley Research Initiative for Sustainable Energy (SinBeRISE), and the Ministry of Education, Singapore for funding under the AcRF grants. One author (S. Shukla), acknowledges the Interdisciplinary Graduate School, NTU for the award a research scholarship.

References

- [1] V. Fthenakis, *Renewable and Sustainable Energy Reviews*, vol. 13, pp 2746-2750, 2009.
- [2] T. M. Razykov, C. S. Ferekides, D. Morel, E. Stefanakos, H. S. Ullal, H.M. Upadhyaya, *Solar Energy*, vol. 85, pp. 1580-1608, 2011.
- [3] T. Unold, H. W. Schock, *Annual Review of Materials Research*, vol. 41, pp. 297-321, 2011.
- [4] A. Ennaoui, S. Fiechter, C. Pettenkofer, N. Alonso-Vante, K. B ker, M. Bronold, C. H pfner, H. Tributsch, *Solar Energy Materials and Solar Cells*, vol. 29, pp. 289-370, 1993.
- [5] M. Cab n-Acevedo, N. S. Kaiser, C. R. English, D. Liang, B. J. Thompson, H. E. Chen, K. J. Czech, J. C. Wright, R. J. Hamers, S. Jin, *Journal of the American Chemical Society*, vol. 136, pp. 17163-17179, 2014.
- [6] D. Liang, M. Cab n-Acevedo, N. S. Kaiser, S. Jin, *Nano Letters*, vol. 14, pp. 6754-6760, 2014.
- [7] M. Limpinsel, N. Farhi, N. Berry, J. Lindemuth, C. L. Perkins, Q. Lin, M. Law, *Energy & Environmental Science*, vol. 7, pp. 1974-1989, 2014.

- [8] J. Puthussery, S. Seefeld, N. Berry, M. Gibbs, M. Law, *Journal of the American Chemical Society*, vol. 133, pp. 716-719, 2011.
- [9] C. Wadia, Y. Wu, S. Gul, S.K. Volkman, J. Guo, A.P. Alivisatos, *Chemistry of Materials*, vol. 21, pp. 2568-2570, 2009.
- [10] M. Gong, A. Kirkeminde, S. Ren, *Scientific Reports*, vol. 3, pp. 2092, 2013.
- [11] G. Hu, L. Hai, R. R. Prabhakar, Y. M. Lam, T. Sritharan, *RSC Advances*, vol. 4, pp. 16489-16496, 2014.
- [12] M. V. Kovalenko, M. Scheele, D. V. Talapin, *Science*, vol. 324, pp. 1417-1420, 2009.
- [13] M. Gong, A. Kirkeminde, Y. Xie, R. Lu, J. Liu, J.Z. Wu, S. Ren, *Advanced Optical Materials*, vol. 1, pp. 78-83, 2013.
- [14] A. Kirkeminde, R. Scott, S. Ren, *Nanoscale*, vol. 4, pp. 7649-7654, 2012.
- [15] D. Y. Wang, Y. T. Jiang, C. C. Lin, S. S. Li, Y. T. Wang, C. C. Chen, C. W. Chen, *Advanced Materials*, vol. 24, pp. 3415-3420, 2012.
- [16] Y. C. Wang, D. Y. Wang, Y. T. Jiang, H. A. Chen, C. C. Chen, K. C. Ho, H. L. Chou, C. W. Chen, *Angewandte Chemie International Edition*, vol. 52, pp. 6694-6698, 2013.
- [17] J. Wu, L. Liu, S. Liu, P. Yu, Z. Zheng, M. Shafa, Z. Zhou, H. Li, H. Ji, Z.M. Wang, *Nano Letters*, vol. 14, pp. 6002-6009, 2014.
- [18] Z. Yang, M. Wang, S. Shukla, Y. Zhu, J. Deng, G. Hu, X. Wang, Q. Xiong, *Scientific Reports*, vol. 5, p. 11377, 2015.
- [19] C. Steinhagen, T. B. Harvey, C. J. Stolle, J. Harris, B. A. Korgel, *The Journal of Physical Chemistry Letters*, vol. 3, pp. 2352-2356, 2012.
- [20] D. R. Alfonso, *The Journal of Physical Chemistry C*, vol. 114, pp. 8971-8980, 2010.
- [21] R. Murphy, D. R. Strongin, *Surface Science Reports*, vol. 64, pp. 1-45, 2009.
- [22] H. A. Macpherson, C. R. Stoldt, *ACS Nano*, vol. 6, pp. 8940-8949, 2012.
- [23] S. Shukla, G. Xing, G. Hu, R. R. Prabhakar, S. Mathew, Z. Su, V. Nalla, T. Venkatesan, N. Mathews, T. Sritharan, T. C. Sum, Q. Xiong, *ACS Nano*, vol. 10, pp. 4431-4440, 2016.
- [24] M. Birkholz, S. Fiechter, A. Hartmann, H. Tributsch, *Physical Review B*, vol. 43, pp. 11926-11936, 1991.
- [25] J. L. Verble, R. F. Wallis, *Physical Review*, vol. 182, pp. 783-789, 1969.
- [26] S. Shukla, N. H. Loc, P. P. Boix, T. M. Koh, R. R. Prabhakar, H. K. Mulmudi, J. Zhang, S. Chen, C. F. Ng, C. H. Huan, N. Mathews, T. Sritharan, Q. Xiong, *ACS Nano*, vol. 8, pp. 10597-10605, 2014.
- [27] S. Ushioda, *Solid State Communications*, vol. 10, pp. 307-310, 1972.
- [28] M. Cabán-Acevedo, M. S. Faber, Y. Tan, R.J. Hamers, S. Jin, *Nano Letters*, vol. 12, pp. 1977-1982, 2012.
- [29] M. Birkholz, A. Hartmann, S. Fiechter, H. Tributsch, "Defect Chemistry and Homogeneity Range of Pyrite and Their Influence on the Optoelectronics Behaviour," in *Proceedings Tenth E.C. Photovoltaic Solar Energy Conference*, Springer Netherlands, pp. 96-99, 1991.
- [30] B. Meester, L. Reijnen, A. Goossens, J. Schoonman, *Chemical Vapor Deposition*, vol. 6, pp. 121-128, 2000.
- [31] M. Birkholz, D. Lichtenberger, C. Höpfner, S. Fiechter, *Solar Energy Materials and Solar Cell*, vol. 27, pp. 243-251, 1992.
- [32] G. Willeke, R. Dasbach, B. Sailer, E. Bucher, *Thin Solid Films*, vol. 213, pp. 271-276, 1992.
- [33] L. Vadkhiya, B.L. Ahuja, *Journal of Alloys and Compounds*, vol. 509, pp. 3042-3047, 2011.
- [34] V. N. Antonov, L. P. Germash, A. P. Shpak, A. N. Yaresko, *Physica Status Solidi (b)*, vol. 246, pp. 411-416, 2009.
- [35] A. Popov, *Pan Stanford, Singapore*, 2011.
- [36] K. M. G. Unger, *Amorphous semiconductors, Topics in Applied Physics*, vol. 36. Springer-Verlag Berlin, 1979.
- [37] K. Aravind, F. W. Herbert, Y. Sidney, J. V. V. Krystyn, Y. Bilge, *Journal of Physics: Condensed Matter*, vol. 25, no. 045004, 2013.
- [38] J. Hu, Y. Zhang, M. Law, R. Wu, *Physical Review B*, vol. 85, no. 085203, 2012.
- [39] K. A. Shore, *Contemporary Physics*, vol. 55, pp. 337-337, 2014.
- [40] U. Nandi, D. Jana, D. Talukdar, *Progress in Materials Science*, vol. 71, pp. 1-92, 2015.
- [41] M. Cabán-Acevedo, D. Liang, K. S. Chew, J. P. DeGrave, N. S. Kaiser, S. Jin, *ACS Nano*, vol. 7, pp. 1731-1739, 2013.
- [42] P. A. Montano, M. S. Seehra, *Solid State Communications*, vol. 20, pp. 897-898, 1976.
- [43] P. Burgardt, M. S. Seehra, *Solid State Communications*, vol. 22, pp. 153-156, 1977.